



Metal recovery based magnetite near-infrared photocatalyst with broadband spectrum utilization property

Shouqiang Huang, Haoming Wang, Nanwen Zhu*, Ziyang Lou, Liang Li, Aidang Shan, Haiping Yuan

School of Environmental Science and Engineering, Shanghai Jiao Tong University, 800 Dongchuan Road, Shanghai 200240, PR China

ARTICLE INFO

Article history:

Received 14 June 2015

Received in revised form 1 August 2015

Accepted 9 August 2015

Available online 12 August 2015

Keywords:

Magnetite

Photocatalyst

Near-infrared light

Upconversion

Electroplating wastewater

ABSTRACT

Magnetite near-infrared (NIR) photocatalysts with upconversion properties are put forward to meet the requirements of high solar energy utilization efficiency and sustainability based on the resource utilization of electroplating wastewater (EPW). The Ca–Zn magnetite precursor (CZ) was initially prepared from the mixed-ferrites (M-Fe₃O₄) produced from EPW and the photocatalyst (Zn²⁺) and upconversion host material (Ca²⁺)-related metal ions included in EPW and its effluents. With the addition of lanthanides and F[−] ions, a novel magnetite NIR photocatalyst of Er³⁺/Tm³⁺/Yb³⁺–(CaF₂/ZnFe₂O₄/ZnO) (ETY-FCZ) was further synthesized. In the crystal phases of ETY-FCZ, (Ca_{0.8}Yb_{0.2})F_{2.2} is used as the upconversion host material for Er³⁺/Tm³⁺/Yb³⁺ ions. The magnetic agents including ZnFe₂O₄ display the heterojunction with ZnO, as well as the broadband spectrum utilization property for ETY-FCZ. ETY-FCZ possesses efficient electron-hole pair separation ability, and all the upconversion luminescence emitted from ETY-FCZ can be absorbed for photocatalysis, which result in higher removal rates of methyl orange and salicylic acid compared to those of CZ. ETY-FCZ is an excellent magnetite NIR photocatalysts with magnetic recycling performance, and it has promising applications in the reuse of EPW and the wastewater treatment.

© 2015 Elsevier B.V. All rights reserved.

1. Introduction

Upconversion assisted near-infrared (NIR) photocatalyst powders possess the advantages of good dispersibility in water, large contacted area with pollutants, and highly efficient photocatalytic activities [1,2]. Due to the conversion of NIR light to visible and UV light [3], NIR photocatalysts are becoming the emerging materials to meet the high utilization efficiencies of solar light energy. However, these NIR photocatalysts suffer from a common problem: the recovery of them from the reaction mixtures [4]. To overcome this problem, the introduction of magnetic nanoparticles can be a viable solution for the separation of NIR photocatalysts with an external magnetic field [5].

For the purpose of magnetic separation, ferrite (Fe₃O₄) nanoparticles are widely chosen in the magnetite photocatalysts [6,7], while most of the ferrites used are prepared from pure iron source with the disadvantages of low yields and high costs. To obtain an abundant low cost of ferrites, the resource utilization methods have been applied in the treatment of waste materials, i.e., electroplating

wastewater (EPW) [8], electroplating sludge [9], groundwater treatment sludge [10], red mud in alumina refineries [11], and acid mine drainage [12]. Nevertheless, there are high amounts of metal ions included in EPW, and the “Ferrite process” has been proven to be the effective way for treating EPW [13]. The mixed spinel structure ferrites (M-Fe₃O₄) produced from EPW display high saturation magnetization and nanoscale size. Importantly, most of M-Fe₃O₄, i.e., ZnFe₂O₄ [14,15], CuFe₂O₄ [16], or Ca₂Fe₂O₅ [17] are attributed to the narrow band gap semiconductors. Thus, the integration of M-Fe₃O₄ with semiconductors can form the magnetite photocatalysts with large absorption edges. Meanwhile, EPW includes several photocatalyst-related metal ions, such as Zn²⁺, Ni²⁺, Fe²⁺, and Cu²⁺ ions. With the incorporation of M-Fe₃O₄ into the corresponding photocatalysts of ZnO, NiO, Fe₂O₃, or CuO from EPW can form the magnetite photocatalysts, and M-Fe₃O₄–ZnO exhibits the best photocatalytic activity among them [8].

In the actual treatment process, the pH of EPW is often adjusted by quicklime (CaO), since its cost is lower than that of sodium hydroxide (NaOH). Thus, there are many Ca²⁺ ions in the resulted electroplating effluents and the electroplating sludges. Coincidentally, this part of Ca²⁺ ions can be used to generate CaF₂ by adding F[−] ions, and it is the precondition for the synthesis of CaF₂-based NIR photocatalysts [2,18].

* Corresponding author. Fax: +86 21 54743710.

E-mail address: nwzhu@sjtu.edu.cn (N. Zhu).

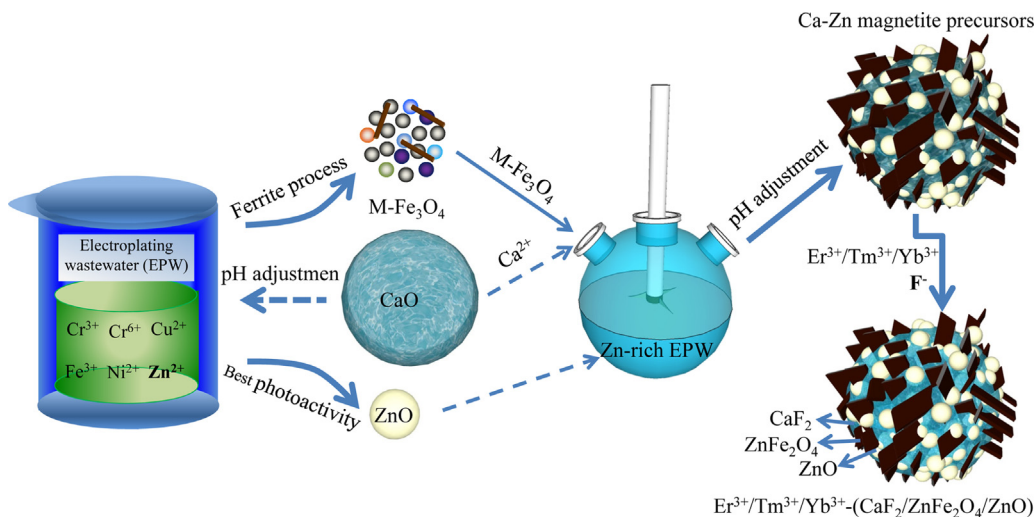


Fig. 1. Schematic illustration for the formation of ETY-FCZ.

In this work, the $M\text{-Fe}_3\text{O}_4$ magnetic agents prepared from the simulated-EPW in our previous work [8] with the $\text{FeSO}_4 \cdot 7\text{H}_2\text{O}:\text{Cr}^{6+}$ mass ratio of 50:1 were introduced into the solution containing Zn^{2+} and Ca^{2+} ions, and the Ca–Zn magnetite precursor (CZ) was initially fabricated, as shown in Fig. 1. Through the comparison of the metal oxide photocatalysts ZnO , NiO , Fe_2O_3 , and CuO [8], it can be found that ZnO exhibits the best photocatalytic activity, and thus the Zn-rich EPW was considered to synthesize ZnO -NIR photocatalysts without adding TiO_2 . With the introduction of Er^{3+} , Tm^{3+} , Yb^{3+} , and F^- ions into CZ, a novel NIR photocatalysts of $\text{Er}^{3+}/\text{Tm}^{3+}/\text{Yb}^{3+}$ -($\text{CaF}_2/\text{ZnFe}_2\text{O}_4/\text{ZnO}$) (ETY-FCZ) was finally obtained. The $M\text{-Fe}_3\text{O}_4$ in ETY-FCZ mainly present with the phase of ZnFe_2O_4 , which could not only construct the heterostructure with ZnO , but also provide broadband spectrum utilization ability for ETY-FCZ. All the upconversion luminescence emitted by the upconversion agent $\text{Er}^{3+}/\text{Tm}^{3+}/\text{Yb}^{3+}$ - CaF_2 in ETY-FCZ could be absorbed for photocatalysis. The photocatalytic abilities of CZ and ETY-FCZ were evaluated by the degradations of methyl orange (MO) and salicylic acid (SA) under NIR and visible-NIR (Vis-NIR) light irradiations.

2. Experimental methods

2.1. Chemicals and materials

$\text{Er}(\text{NO}_3)_3 \cdot 5\text{H}_2\text{O}$, $\text{Tm}(\text{NO}_3)_3 \cdot 5\text{H}_2\text{O}$, $\text{Yb}(\text{NO}_3)_3 \cdot 5\text{H}_2\text{O}$, $\text{Ca}(\text{NO}_3)_2 \cdot 4\text{H}_2\text{O}$, $\text{Zn}(\text{NO}_3)_2 \cdot 6\text{H}_2\text{O}$, and $\text{Ca}(\text{OH})_2$ were used as received without further purification.

2.2. Preparation of CZ

0.04 mol $\text{Ca}(\text{NO}_3)_2 \cdot 4\text{H}_2\text{O}$ and 0.04 mol $\text{Zn}(\text{NO}_3)_2 \cdot 6\text{H}_2\text{O}$ were dissolved in a three-necked flask containing 200 mL distilled water. 1.5 g of the $M\text{-Fe}_3\text{O}_4$ magnetic agents prepared with the $\text{FeSO}_4 \cdot 7\text{H}_2\text{O}:\text{Cr}^{6+}$ mass ratio of 50:1 [8] were chosen and added in the above Ca–Zn mixture with continuous mechanical stirring. The pH of the obtained mixture was adjusted to 10 by adding NaOH (0.3 mol/L), and then the mixture was kept at 80°C for 5 h under stirring at 200 rpm. The precipitates were separated and washed through centrifugation with distilled water and ethanol, and dried in a vacuum at 60°C for 12 h. The resulted powders were calcined at 500°C for 4 h under the protection of flowing argon to obtain the CZ samples.

2.3. Preparation of ETY-FCZ

In a typical procedure of ETY-FCZ, CZ (0.5 g), $\text{Er}(\text{NO}_3)_3 \cdot 5\text{H}_2\text{O}$, $\text{Tm}(\text{NO}_3)_3 \cdot 5\text{H}_2\text{O}$, and $\text{Yb}(\text{NO}_3)_3 \cdot 5\text{H}_2\text{O}$ were added into a three-necked flask containing 100 mL distilled water with continuous mechanical stirring, and the pH was adjusted to 1 by adding nitric acid. The molar ratio of $\text{Ca}^{2+}:\text{Er}^{3+}:\text{Tm}^{3+}:\text{Yb}^{3+}$ was 1:0.02:0.01:0.3. After stirring for 30 min, 40 mL of NaF solution (0.175 mol/L) was added dropwise into the above mixture. Then, the mixture was kept at 80°C for 8 h under stirring at 200 rpm. Excess F^- ions were used to ensure all the Ca^{2+} ions in CZ could be converted to CaF_2 . The precipitates via centrifugation and drying were calcined at 500°C for 4 h under argon protection to form the ETY-FCZ sample (Fig. 1). For comparison purposes, $\text{CaF}_2/\text{ZnFe}_2\text{O}_4/\text{ZnO}$ (FCZ), $\text{Er}^{3+}/\text{Tm}^{3+}/\text{Yb}^{3+}$ -CZ (ETY-CZ), and $\text{Er}^{3+}/\text{Tm}^{3+}/\text{Yb}^{3+}$ - CaF_2 (ETY-C) were also synthesized following the same procedures. In particular, for the fabrication of ETY-C, 0.5 g of $\text{Ca}(\text{OH})_2$ was used as the calcium source to follow the composition and the added amount of CZ.

2.4. Characterization

The X-ray diffraction (XRD) patterns of the samples were performed on a Bruker D8 Advance X-ray Diffractometer at 40 kV and 40 mA using $\text{Cu K}\alpha$ radiation ($\lambda = 1.5406 \text{ \AA}$). The magnetic properties were measured by the Physical Property Measurement System (PPMS-9T, Quantum Design, USA). The morphologies and microstructures were characterized with the Sirion 200 field emission scanning electron microscope (FESEM) equipped with the INCA X-Act energy-dispersive spectroscopy (EDS) instrument and the JEM-2100F transmission electron microscope (TEM). The Brunauer–Emmett–Teller (BET) specific surface areas of the samples were determined on a Quantachrome Autosorb-IQ gas adsorption apparatus at 77 K. The surface composition was measured using the X-ray photoelectron spectroscopy (XPS, Kratos Axis UltraDLD), and the C 1s peak at 284.8 eV was taken as internal reference. The light absorption spectra were detected on the Lambda 750 UV–vis–NIR (Ultraviolet–visible–Near Infrared) spectrophotometer. Upconversion luminescence spectra and photoluminescence (PL) spectra were recorded on a Hitachi F-7000 fluorescence spectrophotometer with a 980 nm semiconductor solid laser.

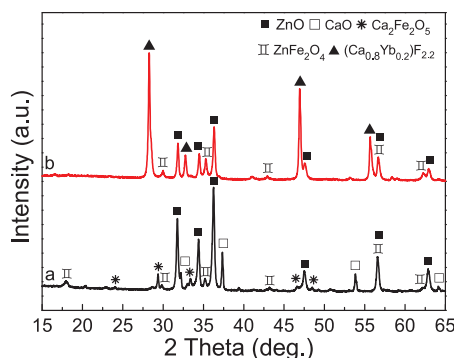


Fig. 2. Typical XRD patterns of (a) CZ and (b) ETY-FCZ.

2.5. Photocatalytic activities

MO and SA degradation experiments were used to evaluate the photocatalytic activities of CZ and ETY-FCZ under NIR ($\lambda \geq 780$ nm) and Vis-NIR ($\lambda \geq 400$ nm) irradiations provided by a 1000 W high pressure mercury lamp. 20 mg of the samples were dispersed in 20 mL of MO or SA aqueous solutions (10 mg/L). Prior to irradiation, the suspensions were kept in the dark for 2 h with mechanical stirring to attain adsorption/desorption equilibrium. Every 30 min intervals, 2.0 mL of the suspensions were collected and analyzed by a UV–vis spectrophotometer (Hitachi U-3900).

3. Results and discussion

3.1. XRD analysis

The XRD patterns of CZ and ETY-FCZ are shown in Fig. 2. As shown in Fig. 2a, the crystal phases of CZ mainly consist of ZnO, CaO, $\text{Ca}_2\text{Fe}_2\text{O}_5$, and ZnFe_2O_4 . In the fabrication process of CZ, there is an excess amount of Fe in $\text{M-Fe}_3\text{O}_4$, and the added Ca^{2+} and Zn^{2+} ions can be reacted with Fe-oxides to form $\text{Ca}_2\text{Fe}_2\text{O}_5$ and ZnFe_2O_4 . The diffraction peaks of ZnO are mainly located at 31.75° , 34.39° , 36.23° , 47.50° , and 56.57° , which match well with the (10 $\bar{1}0$), (0002), (101), (10 $\bar{1}2$), and (11 $\bar{2}0$) planes (JCPDS Card No. 80-0075), respectively. The diffraction peaks at 32.21° , 37.38° , and 53.87° are assigned to the (111), (200), and (220) planes of CaO (JCPDS Card No. 77-2376), respectively. The diffraction peaks at 29.40° , 33.04° , 46.65° , and 48.50° are well indexed to the (131), (200), (202), and (222) planes of $\text{Ca}_2\text{Fe}_2\text{O}_5$ (JCPDS Card No. 71-2264), respectively. The diffraction peaks of ZnFe_2O_4 at 29.86° , 35.24° , and 53.87° are in good accordance with its (220), (311), and (400) planes (JCPDS Card No. 89-7412), respectively. The phase compositions through the Jade reference data of ZnO, CaO, $\text{Ca}_2\text{Fe}_2\text{O}_5$, and ZnFe_2O_4 are 55.8%, 21.8%, 15.4%, and 7.1%, respectively.

After the addition of lanthanides (Er^{3+} , Tm^{3+} , and Yb^{3+}) and F^- ions, the obtained ETY-FCZ contains the phases of $(\text{Ca}_{0.8}\text{Yb}_{0.2})\text{F}_{2.2}$ (JCPDS Card No. 87-0976), ZnO, and ZnFe_2O_4 , and the corresponding phase compositions are 67.3%, 23.3%, and 9.4%, respectively. The CaO and $\text{Ca}_2\text{Fe}_2\text{O}_5$ related diffraction peaks are disappeared, indicating most of their Ca^{2+} ions have been captured by F^- ions to produce CaF_2 . Furthermore, there is an amount of Fe_2O_3 generated from the conversion of $\text{Ca}_2\text{Fe}_2\text{O}_5$ to CaF_2 [19], and this part of Fe_2O_3 will continue to react with ZnO to form ZnFe_2O_4 . Thus, higher amount of ZnFe_2O_4 can be obtained in ETY-FCZ compared to CZ, which will improve the photocatalytic activities through the formation of heterostructure between ZnFe_2O_4 and ZnO.

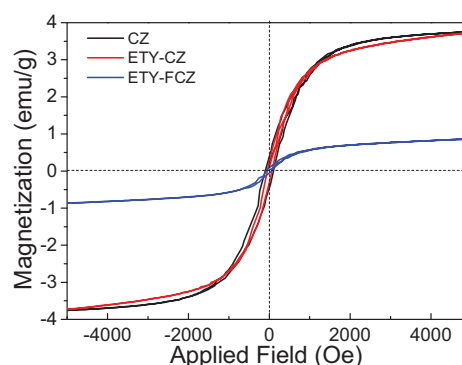


Fig. 3. Room temperature (300 K) magnetic hysteresis curves of CZ, ETY-CZ, and ETY-FCZ.

3.2. Magnetic analysis

The magnetic hysteresis curves of CZ, ETY-CZ, and ETY-FCZ measured at room temperature are shown in Fig. 3 and the corresponding magnetic parameters are listed in Table S1. CZ and ETY-CZ possess the comparative saturated magnetization (M_s), with the values of 3.90 and 4.20 emu/g, respectively. Compared to the high M_s (55.05 emu/g) of $\text{M-Fe}_3\text{O}_4$ [8], the much decreased M_s values in CZ and ETY-CZ are ascribed to their low mass fraction of $\text{M-Fe}_3\text{O}_4$. As for ETY-FCZ, the M_s is continued to decrease to 1.08 emu/g. It is conceivable that the M_s of ETY-FCZ is mainly contributed from ZnFe_2O_4 , and the formation of CaF_2 has reduced the mass fraction of $\text{M-Fe}_3\text{O}_4$. Nevertheless, ETY-FCZ still can be separated by an external magnetic field (Fig. S1).

3.3. Morphologies and microstructures

The morphologies of CZ and ETY-FCZ are examined by SEM and TEM (Fig. 4). CZ includes many near spherical particles with an average size of 1 μm (Fig. 4a and b), and their surfaces are surrounded by many nanoparticles (50–100 nm). The SEM morphologies of ETY-FCZ are shown in Fig. 4c and d, and the sizes of the nanoparticles are not changed much compared to those of CZ, resulting in the comparable BET surface areas (Fig. S2 and Table S2), while the near spherical particles have been aggregated together. The aggregates are investigated by TEM, as shown in Fig. 4e, and it can be found that these aggregates consist of several near spherical particles with an average size of 120 nm. The high-resolution TEM (HRTEM) image of the near spherical particle is shown in Fig. 4f, and the fast Fourier transform (FFT) pattern reveals the (111) and (200) planes with the angle of 55° , denoting that the near spherical particle is attributed to $(\text{Ca}_{0.8}\text{Yb}_{0.2})\text{F}_{2.2}$ with the preferential [011] growth direction. The nanoparticles deposited on the $(\text{Ca}_{0.8}\text{Yb}_{0.2})\text{F}_{2.2}$ particles are further magnified, and the HRTEM image is shown in Fig. 4g. The FFT pattern of the nanosheet crystal (ca. 12 nm) on the right side possesses the (220) and (311) planes with the angle of 31° , which confirms the ZnFe_2O_4 single crystal grew along the [11 $\bar{2}$] direction. On the left side of ZnFe_2O_4 , the (10 $\bar{1}0$) planes of ZnO exist in the FFT pattern. Fig. 4h also shows the HRTEM image of the nanoparticles located at other positions of $(\text{Ca}_{0.8}\text{Yb}_{0.2})\text{F}_{2.2}$. There is a nanosheet crystal on the top of Fig. 4h, and the (422) and (442) planes with an angle of 18° in the FFT pattern represent the ZnFe_2O_4 single crystal. The detected lattice fringe spacing of 0.298 nm is close to its (220) planes. On the bottom of Fig. 4h, the (10 $\bar{1}0$) and (0002) planes with an angle of 90° in the FFT pattern confirm the ZnO single crystal. Thus, the crystal lattices of ZnO and ZnFe_2O_4 are connected to each other, which can form the heterostructure to accelerate the photogenerated electron-hole pair separation. The FFT pattern on the bottom side of Fig. 4i belongs to $(\text{Ca}_{0.8}\text{Yb}_{0.2})\text{F}_{2.2}$ with the (222)

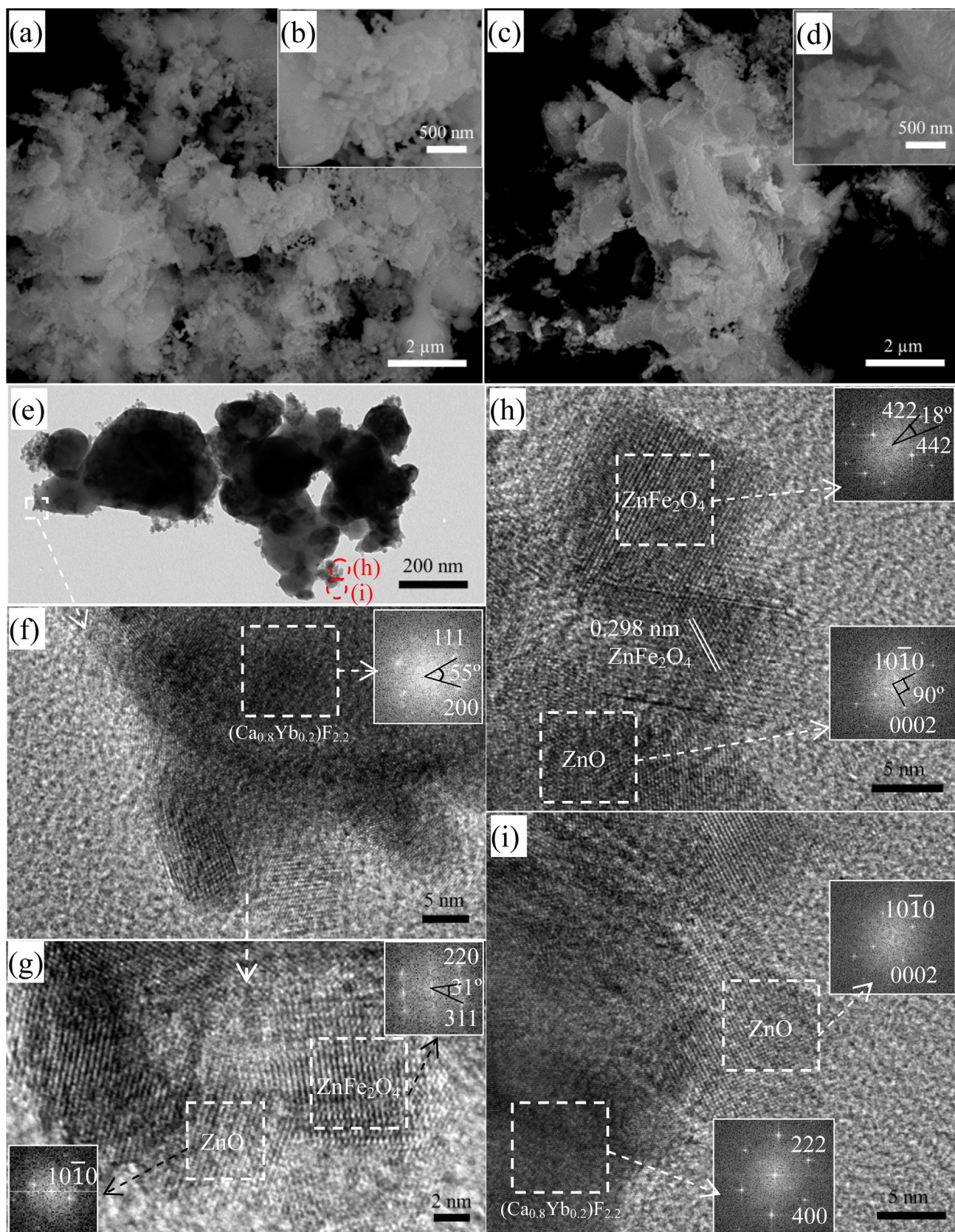


Fig. 4. SEM images of (a and b) CZ. (c and d) SEM, (e) TEM, and (f–i) HRTEM images of ETY-FCZ. Insets: the corresponding fast Fourier transform (FFT) patterns.

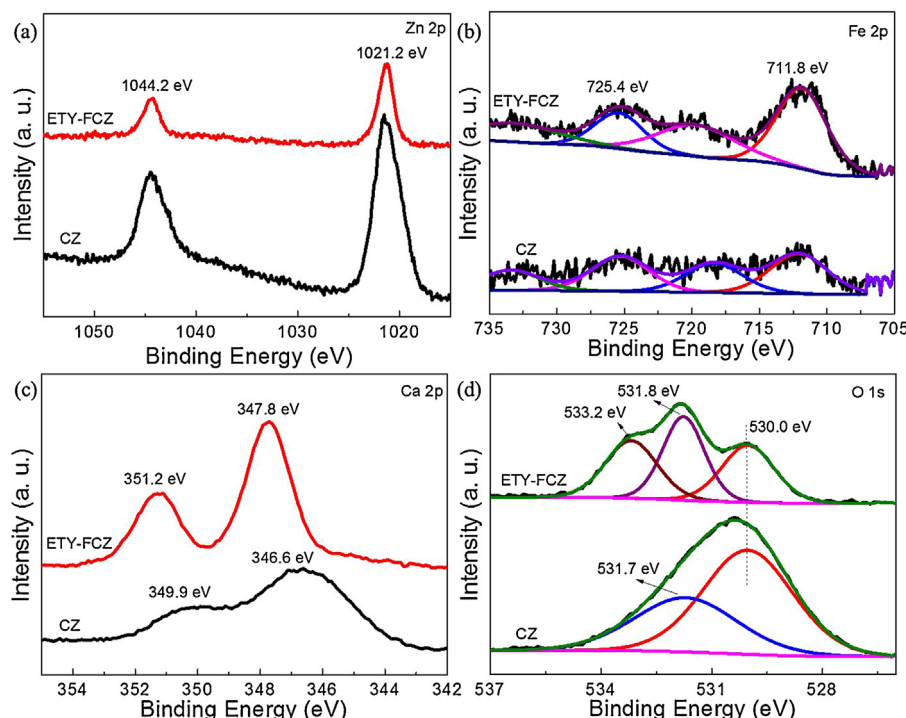


Fig. 5. XPS spectra of CZ and ETY-FCZ: (a) Zn 2p, (b) Fe 2p, (c) Ca 2p, and (d) O 1s.

and (400) planes, and the ZnO crystal is located on the surface of $(\text{Ca}_{0.8}\text{Yb}_{0.2})\text{F}_{2.2}$. Based on the above analysis, it can be found that most of ZnO and ZnFe_2O_4 crystals are deposited on $(\text{Ca}_{0.8}\text{Yb}_{0.2})\text{F}_{2.2}$, indicating that the positions of ZnO and ZnFe_2O_4 are not changed much from the conversion of CaO to CaF_2 , owing that CaF_2 can be in-situ formed from CaO by the introduction of F^- ions.

3.4. Component analysis

Fig. S3a shows the SEM image of CZ. The corresponding EDS spectrum of the selected region A is present in Fig. S3c, and the main elements Zn, Ca, Fe, and O are detected with the atomic ratio of 10.08:6.52:0.59:82.81 (Table S3). The enlarged area of CZ is shown in Fig. S3b. The EDS spectrum of the big particles (Region B) contains the elements Zn, Ca, Fe, and O with the atomic ratio of 4.70:9.72:0.23:85.35. The atomic ratios of Zn, Ca, Fe, and O for the nanoparticles in region C and D are 14.33:2.62:0.62:82.43 and 10.31:5.36:0.56:83.77, respectively. It can be found that the Ca content in the big particles (Region B) is higher than the Zn content, and it is also demonstrated in the EDS spectrum of Region E (Zn:Ca:Fe:O = 4.56:8.42:0.38:86.64). Conversely, the nanoparticles in region C and D possess the higher Zn contents compared to the Ca contents. Therefore, it can be inferred that the big particles are ascribed to CaO, and the nanoparticles consist of ZnO, $\text{Ca}_2\text{Fe}_2\text{O}_5$, and ZnFe_2O_4 . Fig. S3d shows the EDS spectrum of ETY-FCZ, and the elements Zn, Ca, Yb, Er, Tm, Fe, F, and O are detected with the atomic ratio of 23.23:15.29:4.74:0.11:0.04:3.45:17.62:35.52. According to the TEM results of ETY-FCZ (Fig. 4e–i), the nanoparticles of ZnO and ZnFe_2O_4 are deposited on the big particles of $(\text{Ca}_{0.8}\text{Yb}_{0.2})\text{F}_{2.2}$, and it can also be inferred that the big particles in CZ are attributed to CaO due to the in-situ formation of CaF_2 from CaO.

The surface compositions of CZ and ETY-FCZ are detected by XPS, as shown in Figs. S4 and 5. The survey-scan XPS spectra of them (Fig. S4) confirm the main elements of Zn, Fe, Ca, and O elements, and the F and the lanthanide elements (e.g., Yb) are also present in ETY-FCZ. Fig. 5a shows two peaks of Zn 2p at 1044.2 and 1021.2 eV, which correspond to the Zn $2p_{1/2}$ and Zn $2p_{3/2}$ [8], respectively. The Fe 2p

peaks at 725.4 and 711.8 eV (Fig. 5b) are consistent with Fe $2p_{3/2}$ and Fe $2p_{1/2}$ for Fe^{3+} [20,21], respectively. In the Ca 2p spectrum of CZ (Fig. 5c), the peaks at 349.9 (Ca $2p_{1/2}$) and 346.6 eV (Ca $2p_{3/2}$) are assigned to CaO. After the introduction of F^- ions, the peaks of Ca $2p_{1/2}$ and Ca $2p_{3/2}$ are shifted to 351.2 and 347.8 eV, respectively, which are resulted from the formation of CaF_2 [22]. The two fitted binding energy peaks of O 1s at 531.7 and 530.0 eV for CZ (Fig. 5d) are attributed to Ca–O and Zn–O bands [23,24], respectively. In the case of ETY-FCZ, the Ca–O bands are disappeared and substituted by Ca–F bands. The additional peaks of O 1s in ETY-FCZ are detected at 533.2 and 531.8 eV. The O 1s peak at 533.2 eV is attributed to chemisorbed or dissociated oxygen, $-\text{CO}_3$, or OH species on the surface of ETY-FCZ [24,25]. The medium binding energy of O 1s peak at 531.8 eV is consistent with O^{2-} ions located in oxygen-deficient regions of ETY-FCZ, which are produced by the variations of the oxygen vacancy concentrations [26].

3.5. Optical properties

The UV–vis–NIR diffuse reflectance spectra of CZ and ETY-FCZ are shown in Fig. 6, and both of the samples possess the broad-band spectrum utilization ability. The full spectrum absorption can be divided into two parts: the UV light absorption, and the Vis–NIR light absorption. The strong UV light absorption for CZ and ETY-FCZ is originated from ZnO. As has been proposed in the XRD analysis of ETY-FCZ, the reaction between ZnO and Fe_2O_3 can be performed to form ZnFe_2O_4 , and the decreased ZnO content results in lower UV light absorption intensity compared to CZ. The Vis–NIR light absorption for CZ and ETY-FCZ is mainly contributed by $\text{M-Fe}_3\text{O}_4$. The $\text{M-Fe}_3\text{O}_4$ in CZ contains $\text{Ca}_2\text{Fe}_2\text{O}_5$ and ZnFe_2O_4 , while only ZnFe_2O_4 is detected in the $\text{M-Fe}_3\text{O}_4$ of ETY-FCZ. $\text{Ca}_2\text{Fe}_2\text{O}_5$ is an oxygen vacancy-contained perovskite oxide with the band gap energy of about 1.85 eV [27,28]. ZnFe_2O_4 is a normal spinel ferrite with the band gap energy of about 1.88 eV [15,29]. Due to the different ferrites included in CZ and ETY-FCZ, CZ possesses higher absorption in the 540–1120 nm spectral range, while ETY-FCZ has stronger absorption in the spectral range of 390–540 nm, as

well as the spectral range exceeds 1120 nm. Except for the ferrites, the light absorption property of ETY-FCZ is also influenced by the $\text{Er}^{3+}/\text{Tm}^{3+}/\text{Yb}^{3+}$ doped CaF_2 upconversion agent. The UV–vis–NIR diffuse reflectance spectrum of pure ETY-C is shown in Fig. S5a, and the obvious light absorption region located at 900–1000 nm are attributed to the $^2F_{5/2} \rightarrow ^2F_{7/2}$ transitions of Yb^{3+} ions and the $^4I_{11/2} \rightarrow ^4I_{15/2}$ transitions of Er^{3+} ions. Thus, there is also an absorption peak at about 980 nm for ETY-FCZ.

The upconversion luminescence spectra of ETY-FCZ under 980 nm light excitation are shown in Fig. 7. It can be observed that the upconversion emission intensities of ETY-FCZ are enhanced gradually as the output currents increased from 1.0 to 3.0 A (Fig. 7a and b). These upconversion emissions are simultaneously originated from both Er^{3+} and Tm^{3+} ions (Fig. 7c and d). The red (656 nm), green (541 and 523 nm), violet (410 nm), and UV (381 nm) light are attributed to the $^4F_{9/2} \rightarrow ^4I_{15/2}$, $^4S_{3/2} \rightarrow ^4I_{15/2}$, $^2H_{11/2} \rightarrow ^4I_{15/2}$, $^2H_{9/2} \rightarrow ^4I_{15/2}$, and $^4G_{11/2} \rightarrow ^4I_{15/2}$ transitions of Er^{3+} ions [30,31], respectively. The blue (485 nm) and UV (361 nm) light are produced by the $^1G_4 \rightarrow ^3H_6$ and $^1D_2 \rightarrow ^3H_6$ transitions of Tm^{3+} ions [32], respectively. The $^1G_4 \rightarrow ^3F_4$ transitions of Tm^{3+} ions can also contribute to the red emission [33]. According to the light absorption property of ETY-FCZ, all these upconversion emissions can be utilized. Furthermore, despite the light absorption, the visible and UV light emission intensities of ETY-FCZ are still much stronger than those of ETY-CZ, which are resulted from the efficient upconversion luminescence of ETY-C (Fig. S6) with the low-phonon-energy host material of CaF_2 .

3.6. Photocatalytic activities

The photocatalytic activities of CZ and ETY-FCZ are measured using the degradation of MO under NIR irradiation, as shown in Fig. 8a. The C/C_0 conversion plots of MO are decreased steadily as the irradiation time extended to 180 min, with the removal rates of 9.34% and 13.18% for CZ and ETY-FCZ, respectively. The NIR responsive photocatalytic activity of CZ is ascribed to its full spectrum light absorption property (Fig. 6). With the introduction of Er^{3+} , Tm^{3+} , Yb^{3+} , and F^- ions, higher removal rate is obtained for ETY-FCZ. It is associated with the reason that the NIR light cannot only be

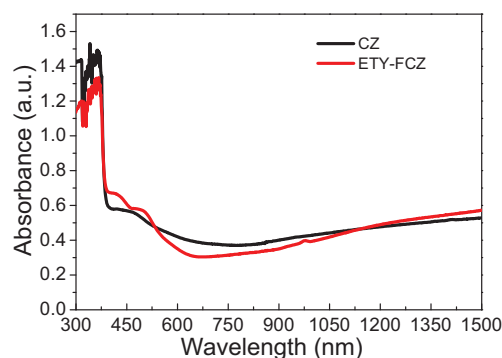


Fig. 6. UV–vis–NIR diffuse reflectance spectra of CZ and ETY-FCZ.

absorbed directly by ETY-FCZ, but also can be upconverted to visible and UV light by $\text{Er}^{3+}/\text{Tm}^{3+}/\text{Yb}^{3+}$ – CaF_2 in ETY-FCZ. In comparison to NIR light, the upconverted visible and UV light can produce the $\cdot\text{OH}$ radicals with stronger oxidation ability to destroy the dye molecular structure [34]. Furthermore, the photocatalytic activity cannot be improved only by the addition of CaF_2 , since the removal rate is decreased to 6.59% over FCZ (Fig. S7), and it demonstrates the important role displayed by the lanthanides.

The Vis–NIR light energy occupies more than 90% in the solar spectrum. To better investigate the advantage of broadband spectrum utilization property, the Vis–NIR driven photocatalytic activities of CZ, FCZ, and ETY-FCZ are further performed. The absorption spectra of SA and MO over ETY-FCZ are shown in Fig. 8b and S8, respectively, and the maximum absorbances of SA at 295 nm and MO at 464 nm are decreased gradually as the irradiation time extended, indicating the continuous decomposition of SA and MO. The C/C_0 conversion plots of SA are shown in Fig. 8c and Fig. S7, and the removal rates of CZ, FCZ, and ETY-FCZ are 50.23%, 13.58%, and 71.9%, respectively. CZ, FCZ, and ETY-FCZ also possess the removal rates of 15.40%, 9.44%, and 43.73% for the MO degradation, respectively. The difference in the SA and MO decompositions may be associated with the selectivities of the samples. However,

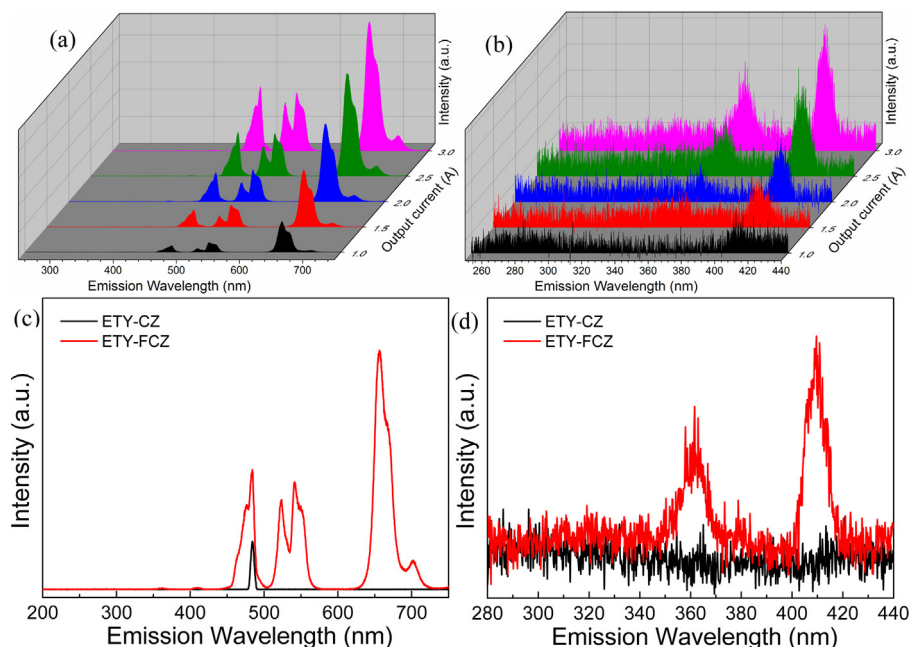


Fig. 7. Upconversion luminescence spectra of (a and b) ETY-FCZ under 980 nm light excitation with different output currents. (c and d) Upconversion luminescence spectra of the samples under 980 nm NIR excitation (output current = 3.0 A).

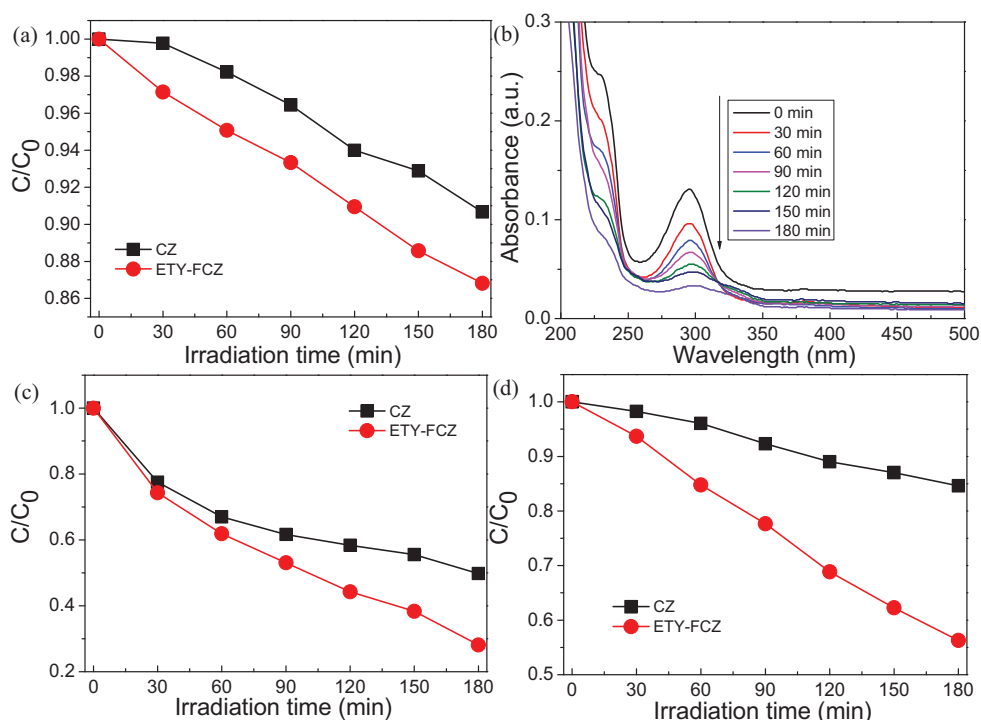


Fig. 8. (a) C/C_0 conversion plots of MO over CZ and ETY-FCZ under NIR light irradiation. Time-dependent absorption spectra of (b) SA over ETY-FCZ under Vis-NIR light irradiation. C/C_0 conversion plots of (c) SA and (d) MO for CZ and ETY-FCZ under Vis-NIR light irradiation.

both the SA and MO degradation performances over ETY-FCZ are better than CZ and FCZ (Fig. S9).

3.7. Photocatalytic mechanisms

The proposed degradation mechanism is shown in Fig. 9. The NIR energy is mainly absorbed by the sensitizers of Yb^{3+} ions, and then the absorbed energy transfers from Yb^{3+} to Er^{3+} and Tm^{3+} to emit the red (656 nm), green (541 and 523 nm), blue (485 nm), violet (410 nm), and UV (381 and 361 nm) light. According to the band gap energies of ZnO (3.2 eV) [35] and ZnFe_2O_4 (1.88 eV) [15], the UV light can directly excite ZnO and ZnFe_2O_4 to generate the electron and hole pairs. The red, green, blue, and violet light can also

be harvested by ZnFe_2O_4 . Based on the HRTEM image of Fig. 4g, the (10 $\bar{1}$ 0) planes of ZnO are connected to the (3 1 1) planes of ZnFe_2O_4 to form the heterostructure. The potentials of the conduction band (CB) and the valance band (VB) edges are calculated according to Mulliken electronegativity theory [36,37]. The obtained E_{VB} values of ZnO and ZnFe_2O_4 are 2.9 eV and 1.49 eV [35], respectively. Meanwhile, the E_{CB} values of ZnO and ZnFe_2O_4 are -0.3 eV and -0.39 eV [15,29], respectively. Thus, the electrons generated on the CB of ZnFe_2O_4 can be transferred to the lower CB edge of ZnO, and the holes of ZnO can be transferred to the VB edge of ZnFe_2O_4 , which will promote the electron-hole pair separation.

As shown in Table S2, the difference between the BET surface areas of CZ and ETY-FCZ is not obvious, whereas the average

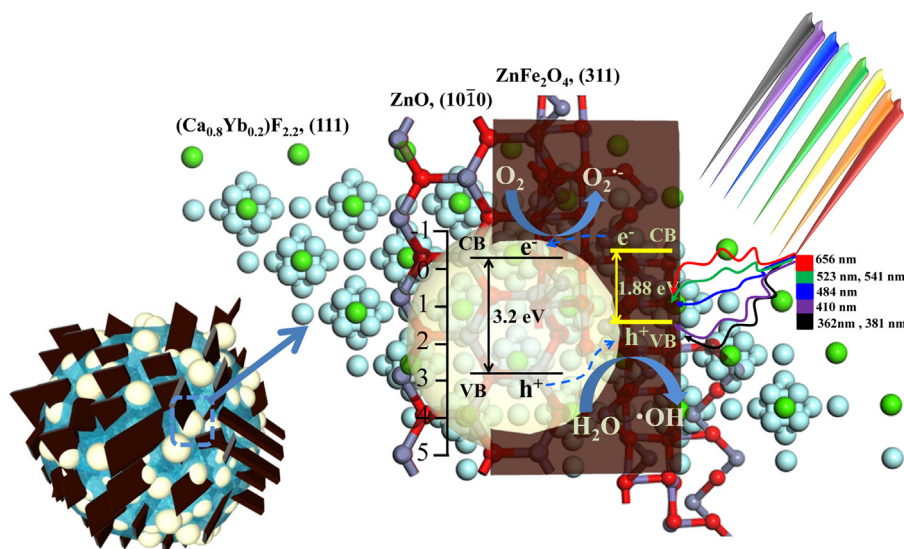


Fig. 9. Schematic illustration of energy transfer mechanism for the photocatalytic reaction process over ETY-FCZ under NIR irradiation.

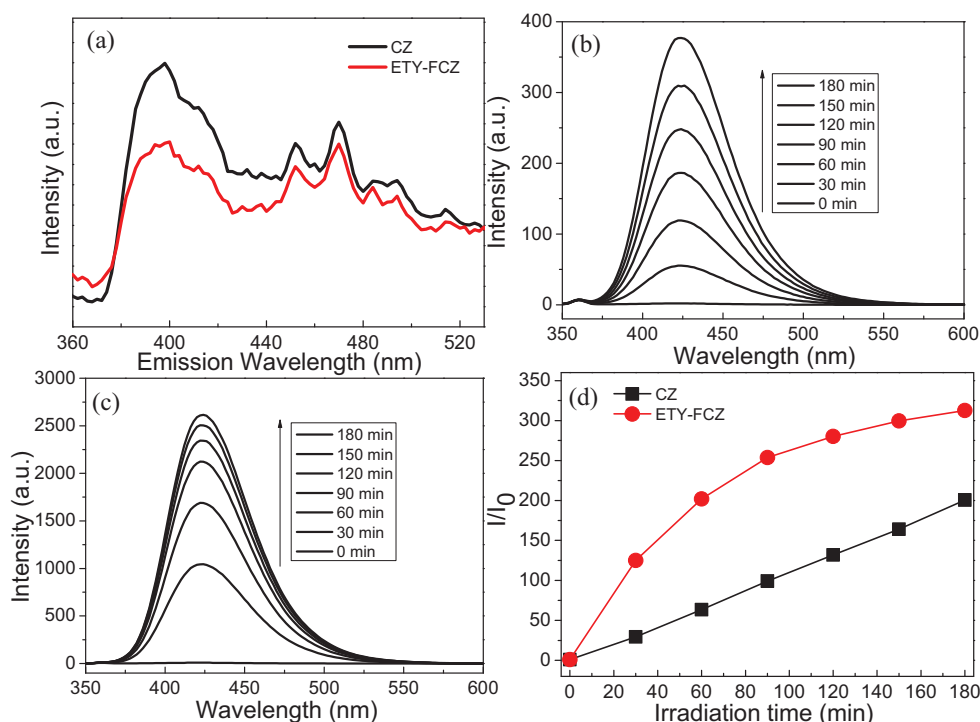


Fig. 10. (a) PL emission spectra of CZ and ETY-FCZ excited at 300 nm. $\cdot\text{OH}$ trapping fluorescence spectra of the terephthalic acid solution containing (b) CZ and (c) ETY-FCZ under Vis-NIR ($\lambda \geq 400$ nm) light irradiation. (d) Time-dependent $\cdot\text{OH}$ productions over the samples under Vis-NIR ($\lambda \geq 400$ nm) light irradiation.

pore size of ETY-FCZ is larger than that of CZ, meaning the higher amounts of MO or SA molecules can be accommodated in ETY-FCZ. The higher pore volume of ETY-FCZ can also result in the more efficient transport pathways compared to CZ for the molecular trafficking [38]. These textural properties of ETY-FCZ are favorable for the improvement of the photocatalytic activities. Fig. 10a shows the PL spectra of CZ and ETY-FCZ at 300 nm excitation. ETY-FCZ possesses lower PL emission intensity compared to CZ, indicating its higher electron-hole pair separation efficiency. It is attributed to the effects resulted from the higher amount of oxygen vacancies (Fig. 5d) [39], as well as the added Er^{3+} , Tm^{3+} , and Yb^{3+} ions, and the formed CaF_2 in ETY-FCZ. The photogenerated electrons can be trapped by the trivalent lanthanides (Er^{3+} , Tm^{3+} , and Yb^{3+}) to form divalent lanthanides [40–42]. Thus, the charge carrier separation is enhanced, which will provide better NIR-driven photocatalytic activity for ETY-FCZ compared to CZ. Furthermore, the upconversion property and the efficient electron-hole pair separation of ETY-FCZ are expected to produce more radicals to destroy the SA and MO molecules. The Vis-NIR driven $\cdot\text{OH}$ trapping fluorescence spectra of the terephthalic acid solution containing CZ and ETY-FCZ are shown in Fig. 10b and c, respectively. As the irradiation time extended, the maximum emission peaks (423 nm) of the 2-hydroxyterephthalic acid increase continuously, while ETY-FCZ has a much stronger ability to generate $\cdot\text{OH}$ radicals (Fig. 10d), and thus the better photocatalytic activities are displayed compared to CZ.

4. Conclusions

With the introduction of the M- Fe_3O_4 magnetic agents obtained from EPW, a magnetite precursor of CZ containing ZnO, CaO, $\text{Ca}_2\text{Fe}_2\text{O}_5$, and ZnFe_2O_4 is obtained. Based on CZ, a novel magnetite NIR photocatalyst of ETY-FCZ is synthesized following a simple sol-gel method. The crystal phases of ETY-FCZ consist of $(\text{Ca}_{0.8}\text{Yb}_{0.2})\text{F}_{2.2}$, ZnO, and ZnFe_2O_4 , and the $(\text{Ca}_{0.8}\text{Yb}_{0.2})\text{F}_{2.2}$ particles are surrounded by the ZnO and ZnFe_2O_4 nanoparticles. ETY-FCZ possesses the broadband spectrum absorption ability, and all the upconverted

light including the red (656 nm), green (541 and 523 nm), blue (485 nm), violet (410 nm), and UV (381 and 361 nm) light emitted by $\text{Er}^{3+}/\text{Tm}^{3+}/\text{Yb}^{3+}$ - CaF_2 can be utilized by ETY-FCZ. Under NIR and Vis-NIR light irradiations, ETY-FCZ exhibits better photocatalytic activities compared to CZ, which are resulted from its upconversion property and the higher electron-hole pair separation efficiency.

Acknowledgements

This work was supported by the Science and Technology Commission of Shanghai Municipality (no. 14DZ1207306), the Shanghai Rising-Star Program (no. 14QA1402400), the National Key Technology R and D Program (no. 2014BAL02B03-4), and Shanghai Tongji Gao Tingyao Environmental Science and Technology Development Foundation.

Appendix A. Supplementary data

Supplementary data associated with this article can be found, in the online version, at <http://dx.doi.org/10.1016/j.apcatb.2015.08.015>

References

- [1] W. Wang, M.Y. Ding, C.H. Lu, Y.R. Ni, Z.Z. Xu, *Appl. Catal. B* 144 (2014) 379–385.
- [2] S.Q. Huang, L. Gu, C. Miao, Z.Y. Lou, N.W. Zhu, H.P. Yuan, A.D. Shan, *J. Mater. Chem. A* 1 (2013) 7874–7879.
- [3] W.Q. Fan, H.Y. Bai, W.D. Shi, *CrystEngComm* 16 (2014) 3059–3067.
- [4] G.Y. Chen, H. Agren, T.Y. Ohulchanskyy, P.N. Prasad, *Chem. Soc. Rev.* 44 (2015) 1680–1713.
- [5] V. Polshettiwar, R. Luque, A. Fihri, H.B. Zhu, M. Bouhrara, J.M. Basset, *Chem. Rev.* 111 (2011) 3036–3075.
- [6] C.T. Chen, Y.C. Chen, *Anal. Chem.* 77 (2005) 5912–5919.
- [7] S.H. Xuan, W.Q. Jiang, X.L. Gong, Y. Hu, Z.Y. Chen, *J. Phys. Chem. C* 113 (2009) 553–558.
- [8] S.Q. Huang, L. Gu, N.W. Zhu, K.L. Feng, H.P. Yuan, Z.Y. Lou, Y.Q. Li, A.D. Shan, *Green Chem.* 16 (2014) 2696–2705.

- [9] D. Chen, J. Hou, L.H. Yao, H.M. Jin, G.R. Qian, Z.P. Xu, Sep. Purif. Technol. 75 (2010) 210–217.
- [10] S.Y. Zhu, S. Fang, M.X. Huo, Y. Yu, Y. Chen, X. Yang, Z. Geng, Y. Wang, D.J. Bian, H.L. Huo, J. Hazard. Mater. 292 (2015) 173–179.
- [11] M. Samouhos, M. Taxiarchou, P.E. Tsakiridis, K. Potiridis, J. Hazard. Mater. 254 (2013) 193–205.
- [12] W. Mckinnon, J.W. Choung, Z. Xu, J.A. Finch, Environ. Sci. Technol. 34 (2000) 2576–2581.
- [13] M. Erdem, F. Tumen, J. Hazard. Mater. 109 (2004) 71–77.
- [14] A.A. Tahir, K.G.U. Wijayantha, M. Mazhar, V. Mckee, Thin Solid Films 518 (2010) 3664–3668.
- [15] K.J. McDonald, K.S. Choi, Chem. Mater. 23 (2011) 4863–4869.
- [16] H.H. Yang, J.H. Yan, Z.G. Lu, X. Cheng, Y.G. Tang, J. Alloys Compd. 476 (2009) 715–719.
- [17] Y.X. Wang, Y.Q. Wang, Y.T. Gao, React. Kinet. Mech. Cat. 99 (2010) 485–491.
- [18] S.Q. Huang, N.W. Zhu, Z.Y. Lou, L. Gu, C. Miao, H.P. Yuan, A.D. Shan, Nanoscale 6 (2014) 1362–1368.
- [19] B.J. Xue, J. Luo, F. Zhang, Z. Fang, Energy 68 (2014) 584–591.
- [20] Y. Hou, X.Y. Li, Q.D. Zhao, X. Quan, G.H. Chen, Adv. Funct. Mater. 20 (2010) 2165–2174.
- [21] M. Wang, Z.H. Ai, L.Z. Zhang, J. Phys. Chem. C 112 (2008) 13163–13170.
- [22] S. Bahadur, D. Gong, J. Anderegg, Wear 197 (1996) 271–279.
- [23] F. Bebensee, F. Voigts, W. Maus-Friedrichs, Surf. Sci. 602 (2008) 1622–1630.
- [24] P.T. Hsieh, Y.C. Chen, K.S. Kao, C.M. Wang, Appl. Phys. A 90 (2008) 317–321.
- [25] S.S. Karpova, V.A. Moshnikov, A.I. Maksimov, S.V. Mjakin, N.E. Kazantseva, Semiconductors 47 (2013) 1026–1030.
- [26] T. Szörényi, L.D. Laude, I. Bertóti, Z. Kántor, Z. Geretovszky, J. Appl. Phys. 78 (1995) 6211–6219.
- [27] C.B. Azzoni, M.C. Mozzati, V. Massarotti, D. Capsoni, M. Bini, Solid State Sci. 9 (2007) 515–520.
- [28] X.B. Chen, S.H. Shen, L.J. Guo, S.S. Mao, Chem. Rev. 110 (2010) 6503–6570.
- [29] W.Q. Zhang, M. Wang, W.J. Zhao, B.Q. Wang, Dalton Trans. 42 (2013) 15464–15474.
- [30] G.F. Wang, Q. Peng, Y.D. Li, J. Am. Chem. Soc. 131 (2009) 14200–14201.
- [31] F. Wang, X.G. Liu, Chem. Soc. Rev. 38 (2009) 976–989.
- [32] D.X. Xu, Z.W. Lian, M.L. Fu, B.L. Yuan, J.W. Shi, H.J. Cui, Appl. Catal. B 142–143 (2013) 377–386.
- [33] V. Mahalingam, F. Mangiarini, F. Vetrone, V. Venkatramu, M. Bettinelli, A. Speghini, J.A. Capobianco, J. Phys. Chem. C 112 (2008) 17745–17749.
- [34] R. Nakamura, T. Tanaka, Y. Nakato, J. Phys. Chem. B 108 (2004) 10617–10620.
- [35] G.X. Tong, F.F. Du, W.H. Wu, R.N. Wu, F.T. Liu, Y. Liang, J. Mater. Chem. B 1 (2013) 2647–2657.
- [36] J. Jiang, X. Zhang, P.B. Sun, L.Z. Zhang, J. Phys. Chem. C 115 (2011) 20555–20564.
- [37] S.Q. Huang, Y.M. Feng, L.H. Han, W.L. Fan, X. Zhao, Z.Y. Lou, Z.B. Qi, B. Yu, N.W. Zhu, RSC Adv. 4 (2014) 61679–61686.
- [38] S. Rasalingam, C.M. Wu, R.T. Koodali, ACS Appl. Mater. Interfaces 7 (2015) 4368–4380.
- [39] Y. Wang, C.X. Feng, M. Zhang, J.J. Yang, Z.J. Zhang, Appl. Catal. B 104 (2011) 268–274.
- [40] S. Obregón, G. Colón, Chem. Commun. 48 (2012) 7865–7867.
- [41] E. Beurer, J. Grimm, P. Gerner, H.U. Güdel, J. Am. Chem. Soc. 128 (2006) 3110–3111.
- [42] S.M. Kaczmarek, T. Tsuboi, M. Ito, G. Boulon, G. Leniec, J. Phys. Condens. Matter. 17 (2005) 3771.